A MODEL-BASED REGISTRATION APPROACH OF PREOPERATIVE MRI WITH 3D ULTRASOUND OF THE LIVER FOR INTERVENTIONAL GUIDANCE PROCEDURES

S. Kadoury[⋆]*, L. Zagorchev*[⋆]*, B.J. Wood*[†]*, A. Venkatesan*[†]*, J. Weese*[*]*, J. Jago*[‡]*, J. Kruecker*[⋆]

[⋆]Philips Research North America, Briarcliff Manor, NY, USA
[†]Center of Interventional Oncology, National Institutes of Health, Bethesda, MD, USA
[*]Philips Research Europe, Hamburg, Germany; [‡]Philips Healthcare, Bothell, WA, USA

ABSTRACT

In this paper, we present a novel approach to rigidly register intraoperative electromagnetically tracked ultrasound (US) with preoperative contrast-enhanced magnetic resonance (MR) images. The clinical rationale for this work is to allow accurate needle placement during thermal ablations of liver metastases using multimodal imaging. We adopt a model-based approach that rigidly matches segmented liver surface shapes obtained from the multimodal image volumes. Towards this end, a shape-constrained deformable surface model combining the strengths of both deformable and active shape models is used to segment the liver surface from the MR scan. It incorporates *a priori* shape information while external forces guide the deformation and adapts the model to a target structure. The liver boundary is extracted from US by merging a dynamic region-growing method with a graph-based segmentation framework anchored on adaptive priors of neighboring surface points. Registration is performed with a weighted ICP algorithm with a physiological penalizing term. The MR segmentation model was trained with 30 datasets and validated on a separate cohort of 10 patients with corresponding ground truth. The accuracy and robustness of the method were assessed by registering four US/MR datasets, yielding accurate landmark registration errors (3.7 ± 0.69mm) and high robustness, and is thus acceptable for radiofrequency clinical applications.

***Index Terms*—** MRI, ultrasound, surface-based registration, deformable shape models, image-guided liver interventions.

1. INTRODUCTION

Needle-based interventions such as biopsy and image-guided ablations are common clinical procedures for diagnosis and treatment of malignant or potentially malignant lesions in the liver or other soft tissues. These are usually guided by ultrasound (US), and fused with computed tomography (CT) and/or magnetic resonance (MR) imaging based on the identified tumor location using an electromagnetic (EM) tracking system to provide a high resolution and high contrast image with a larger field of view [1]. In that respect, the automated registration of these modalities is an important component to allow for a streamlined workflow and increased clinical adoption.

Various approaches have been described in the literature to address this issue by establishing similarity measures between US and CT or MR. Roche et al. [2] describe an image-based registration method between MRI and 3D US, achieved by using both MRI intensity and gradient information in a similarity criterion based upon the correlation ratio (CR). An alternative method looked at probabilistic maps from US and MR images of the liver, where each pixel was assigned with a probability of belonging to a vessel tree [3, 4]. Milko reported a similar approach by focusing on representing hepatic vessels as 2D probability maps using US dynamics [5]. In cases where the workflow relies on a surface- or feature-based approach, high quality of the segmentation becomes imperative for an accurate registration. However, automatic segmentation in MRI poses a very significant challenge, since MRI typically shows variable contrast and smaller edge magnitude than CT images, thereby complicating the application of purely edge-based segmentation methods. Level-set approaches, either edge or region-based, have shown promise [6] while more recently, probabilistic prior models incorporating intensity distributions demonstrated increased robustness [7]. Still, inter- and intra-patient variations in the boundaries intensity appearance make the surface detection very difficult when empirically determined feature properties are assigned to cost functions.

The objective of this work is to develop an automated liver registration procedure anchored on an unsupervised MR liver segmentation and a patient-specific liver surface extraction from US imaging. The constrast-enhanced MR segmentation uses a shape-constrained deformable surface model combining the strengths of both deformable and active shape models by incorporating *a priori* shape information to segment the liver surface. The proposed US surface extraction does not rely on a static prior shape model given the high variability in breathing motion and liver shape appearance from patient to patient. It is anchored on a graph-cut approach to detect optimal surface boundaries by analyzing local neighboring contrast variations between internal tissue and diaphragm intensity, which in turn are used as priors to achieve a robust extraction.

2. METHODS

The workflow for the procedure is illustrated in Fig. 1. The inputs include the contrast-enhanced MRI and tracked US images from a liver sweep at a probe position denoted as p_{US}. The output is a rigid transformation enabling MR/US image fusion.

2.1. MR Liver Segmentation

Prior to the image-guided intervention, the MR image volume is automatically segmented to obtain a 3D shape model of the liver. A shape-constrained deformable surface model [8] is employed to guide the segmentation from the contrast-enhanced MR scan, denoted as I_{MR}. The model is represented by a triangular mesh which

This work was supported in part by the Intramural Research Program of the National Institutes of Health Clinical Center and by a Collaborative Research and Development Agreement between the National Institutes of Health and Philips Healthcare.

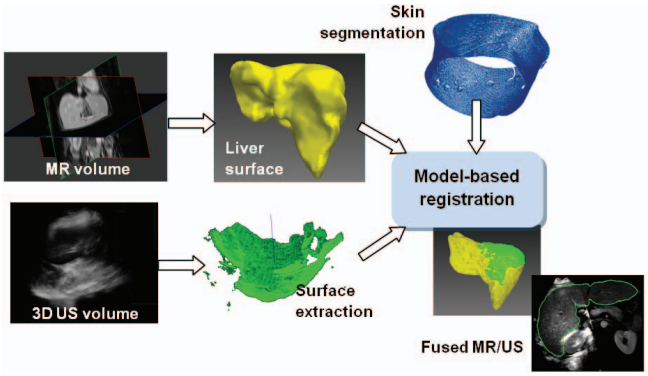


Fig. 1. Flowchart diagram of the proposed MR/US model-based registration approach.

consists of V vertices and T triangles. Every triangle in the model is associated with a feature function F. The goal of the feature function is to identify the optimal target position for a triangle by discriminating between different candidate positions according to an expected boundary appearance. The feature functions are selected and assigned to each triangle in the feature training step based upon a set of ground truth manually segmented volumes. A set of possible feature function candidates is evaluated in terms of accuracy with which the target points are detected in a simulated search. Object boundaries in general can be detected by projecting the image gradient ∇I_{MR} onto the triangle normal $\mathbf{n}$ [9]. This suppresses the effect of edges (high gradients) which deviate from the expected surface orientation. Furthermore, gradients exceeding a certain threshold g_{max} can be damped, yielding:

$$G_{proj}(\mathbf{x}) = (\mathbf{n} \cdot \nabla I_{MR}(\mathbf{x})) \frac{g_{max}^2 + g_{max}||\nabla I_{MR}(\mathbf{x})||}{g_{max}^2 + ||\nabla I_{MR}(\mathbf{x})||^2} \quad (1)$$

where $\mathbf{x}$ represents the vertex coordinates of a target point in the 3D volume. The feature function can be made even more discriminative by encoding additional knowledge that can be used to reject edges if the local image properties violate some criteria as:

$$F(\mathbf{x}) = \begin{cases} \pm G_{proj}(\mathbf{x}) & \text{if } Q_k \in [Min_k, Max_k] \text{ for all } Q_k \in S \\ 0 & \text{otherwise} \end{cases} \quad (2)$$

where S is a set of image quantities Q_k, and $[Min_k, Max_k]$ represents a range of allowed values learned from the training data. If at least one of the image quantities falls outside of the learned range, the edge will be rejected by setting the feature response to 0. The $\pm$ sign accounts for the expected transition of image intensities along the triangle normal (bright-to-dark or dark-to-bright). The adaptation of the model to a volume is guided by the minimization of:

$$E = E_{ext} + \alpha E_{int}. \quad (3)$$

The external energy (E_{ext}) moves the mesh towards detected image boundaries while the internal energy (E_{int}) penalizes deviation from the mean shape model. The parameter α acts as a weighting term that balances the effect of the two energies.

The adaptation is an iterative process that combines a boundary detection step with a deformation step. The boundary detection is accomplished by finding a target point x_i for mesh triangle i such that it maximizes the response of the associated feature function F along the normal of that triangle. The external energy then penalizes the squared distance between each triangle center c_i and the plane tangent to the detected boundary:

$$E_{ext} = \sum_{i=1}^{T} w_i \left(\frac{\nabla I_{MR}(\mathbf{x}_i)}{||\nabla I_{MR}(\mathbf{x}_i)||} \cdot (\mathbf{c}_i - \mathbf{x}_i) \right)^2. \quad (4)$$

The projection of $(\mathbf{c}_i - \mathbf{x}_i)$ onto the image gradient direction allows for sliding of the triangle along the detected image boundary. The weight w_i reflects the response of the feature function F and results in high values for reliably detected boundaries and low values for ill-defined boundaries. The internal energy penalizes the mesh for deviating from the mean shape during adaptation such that:

$$E_{int} = \sum_{j=1}^{V} \sum_{l \in N(j)} ((\mathbf{v}_j - \mathbf{v}_l) - (\mathcal{T}[\mathbf{m}_j] - \mathcal{T}[\mathbf{m}_l]))^2 \quad (5)$$

where $N(j)$ is the set of edge-connected neighbor vertices for vertex j (or $\mathbf{v}_j$), $\mathbf{m}_j$ and $\mathbf{m}_l$ are the coordinates of vertices j and l in the mean mesh, and $\mathcal{T}$ the affine transformation. As defined in (5), the internal energy penalizes deviations in length and orientation for all edges between the mesh during adaptation and the shape model. The model is initialized with a Generalized Hough Transform based on the feature functions F, followed by an affine transformation applied to the global mesh model for pose adaptation. Finally, the deformable adaptation step described above further improves the alignment of the mesh vertices with the corresponding target structures. This generates a triangulated liver surface $\mathbf{S}_{MR\ liver}$ (Fig. 1).

2.2. Graph-based US Liver Surface Extraction

From an input 3D US volume $I_{US}(x, y, z)$ of an EM tracked liver sweep, the liver surface boundary is extracted using a confidence-based region growing algorithm which iteratively creates a binary volume by dynamically adapting the mean μ and standard deviation σ of intensity values in a current region. A seed is automatically generated by a high-intensity voxel selected from the volume's histogram $h(I_{US})$, applied with hard constraints such as minimal distance to the sweep's principal axis w_0, and maximal extent to the probe location p_{US}. The axis w_0 is computed by a principal component analysis (PCA) of the recorded tracking data collected during the sweep. The method iteratively includes voxels based on the criteria $I_{US}(X) \in [\mu - f\sigma, \mu + f\sigma]$, where the automatically determined f factor is a contrast-specific parameter. We define f so the intersection of w_o with the updated segmentation volume $I_{US}(f)$ does not go over a surface thickness t_{thick}, thereby detecting the segmentation to propagate inside the liver hepatic tissue. An inner layer surface extraction method was developed as a subsequent step to obtain a thin surface area of the liver capsule $\mathbf{S}_{US\ liver}$.

By representing the segmented surface $\mathbf{S}_{US\ liver}$ as a terrain-like structure, a node-weighted directed graph $G = (V, E)$ is constructed to propagate and expand the surface, where every node $V(x, y, z) \in V$ represents one and only one voxel in $I_{US}(x, y, z)$, with $V(x, y, z) \in \mathbf{S}_{US\ liver}$, each associated with a cost $c(x, y, z)$. The cost $c(x, y, z)$ assigned to the image voxel $I_{US}(x, y, z)$ can be constructed by minimizing the difference in intensities inside and outside the boundary based on the local a priori measures adapted to the neighborhood N of segmented surface points:

$$c(x, y, z) = \sum_{z \leq z'} (I_{US}(x, y, z') - \eta_1)^2 + \sum_{z > z'} (I_{US}(x, y, z') - \eta_2)^2 \quad (6)$$

where η_1 and η_2 are the mean intensities below and above the liver surface as indicated by z' computed in N such that:

$$\eta_1 = \frac{1}{n_1} \sum_{V(x,y,z)\in V} \sum_{z\leq z'} I_{US}(x,y,z') \tag{7}$$

$$\eta_2 = \frac{1}{n_2} \sum_{V(x,y,z)\in V} \sum_{z> z'} I_{US}(x,y,z') \tag{8}$$

with n_1 and n_2 being the counted number of segmented surface points in N surrounding $V(x,y,z)$ above and below the liver surface respectively. The graph-cut minimization procedure is achieved by maximizing the similarity of new segmented surface points with intensity priors adapted in the local region of a search point.

2.3. Weighted ICP-constrained Registration

A reliable starting point is crucial for avoiding local minima and restricting the search space to anatomically feasible solutions. We propose an approach which uses the tracked US probe as a scan plane selector which clamps to the skin surface segmentation $\mathbf{S}_{MR\ skin}$. An acquisition point p_{init} obtained at any location near the midline of the sternum with the probe placed perpendicularly allows to collect tracking data to estimate translation and rotation parameters (t, R) and automatically determining the caudal-cranial direction.

The minimization term follows an anisotropic weighted ICP objective function, constrained by penalizing potential transformation candidates (6 degrees of freedom (*dof*)) which map probe positions further away from skin surface:

$$\begin{aligned} E^k = \underset{\mathbf{T}_{3DUS\rightarrow MR}}{\operatorname{argmin}} & \sum_{i\in\mathbf{S}_{US\ liver}} \|W_i^k(Rp_i^k + t - q_i^k)\cdot n_i^k\|^2 \\ & + \sum_{j\in R_{MR}} \Psi(R^k_{MR_j}, R^k_{US_j}) \\ & + \Phi(\mathbf{T}, p^k_{US,init}, \mathbf{S}_{MR\ skin}) \end{aligned} \tag{9}$$

where the first term maximizes the alignment of both MR and US point set models, with $q_i^k \in \mathbf{S}_{MR\ liver}$ and n_i^k defined as the normal at each point coordinate of the MR liver model. We account for non-corresponding surface points using the anisotropic distribution W_i^k, which associates covariance matrices of $\mathbf{S}_{MR\ liver}$ and $\mathbf{S}_{US\ liver}$ based on Voronoi regions associated with a vertex [10]. We then incorporate regional salient statistics as a second data-related similarity term Ψ, which seeks to align sub-regions R_{US_j} to corresponding mesh surfaces R_{MR_j}. The similarity based on variability criterions, measures the combinatorial complexity of partial matching of large meshes. We make abstraction of salient geometric features by introducing them as a compound high-level term of non-trivial local shapes. Finally, a cost assigning function Φ is linked to the transformation applied to the US sweep and midline probe locations ($p_{US,init}$). This prevents the EM tracked probe positions acquired on the patient's skin from being mapped further away from the segmentation $\mathbf{S}_{MR\ skin}$. The US probe position p_{US} is linked to an inversely linear function which allows for possible probe pressure being applied during the liver sweep. Since the convexity of the solution domain is not guaranteed, we adopt the widely used multi-resolution registration approach where coarse-to-fine transformation parameters are applied for optimal convergence. Following the gross adjustment, we use a gradient-descent, non-linear Levenberg-Marquardt optimization scheme on all 6 *dof* to determine the optimal solution based on k-step iterative sequential search.

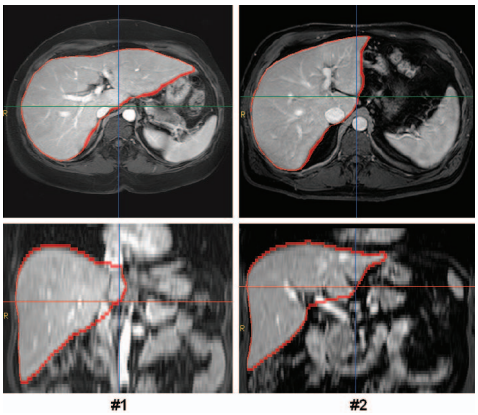
3. RESULTS

The shape-constrained deformable model was trained with a dataset of 30 T1-w contrast-enhanced images from a Philips 1.5T Achieva MR scanner (Philips Medical Systems, Best, The Netherlands), with a 70-sec delay post contrast injection. The average slice resolution was 468×468, the slice number was 68 in average (min 60, max 100). The average pixel size was 0.83×0.83mm, with 8mm slice thickness. Each volume was manually traced to outline the liver boundaries. Quantitative evaluation of the MR segmentation accuracy was carried out in a separate testing population of 10 datasets with manually identified ground truth data. The energy term was set at $\alpha = 7$. For each output segmentation (30s on average), the mean absolute distance (MAD), median error, Hausdorff distance and DICE coefficients were obtained. Table 1 summarizes the evaluation results. The average MAD was of 1.9 ± 0.4mm, while the mean DICE was 93.6% for all cases. Fig. 2 shows the results of the automatic segmentation using the trained model, as well as a the color-coded error maps to the ground truth. One can see the highly accurate modeling of the right liver lobe, in contrast to the left lobe which is more prone to blurred boundaries and motion artifacts.

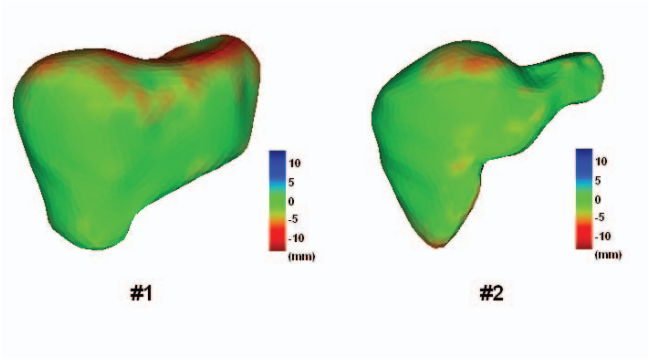
A study on abdominal data from four patients with corresponding MR/US image pairs was conducted in order to evaluate the performance of the registration algorithm in a clinical context. The clinical trial was approved by the institutional investigational review board at our institution, and all patients gave written informed consent. The mean age of the patient population was of 52 ± 7.5. Patients who had one or more malignant or suspicious lesions which were not previously treated were included. An iU22 scanner (Philips Healthcare, Andover, MA) was used for freehand US acquisitions which were acquired at breath-hold. The registration was completed in 44s on average (C++ on an Intel Centrino 2). Ground truth data was obtained manually for both point landmark correspondences such as visible hepatic bifurcations or clips (2-4 per patient) and registration transformations. For the US segmentation, $t_{thick} = 14$. We generated 100 perturbed random initializations and differences in rotation (δ_θ) and translation (δ_t) were computed for all sets. A registration was deemed successful when $\|\delta_\theta\| < 6^\circ$ and $\|\delta_t\| < 8$mm. Table 2 shows these results. The success rate of the proposed new algorithm was 89% on average, with an average landmark registration error (LRE) of 3.75 ± 0.69mm. Fig. 3 illustrates the results.

4. CONCLUSION

An automated registration method aligning US with prior diagnostic MRI using surface shape matching is described, thus enabling image fusion in the context of interventional procedures of the liver. Our main contributions lie first in the training of a shape-constrained deformable model for an unsupervised segmentation of the liver in MR images, followed by a robust surface extraction technique from US using dynamic region growing which adapts to varying image contrast. The former combines the strengths of both deformable and active shape models by encoding *a priori* shape information obtained from training data. Results show accurate MR segmentations in the right liver lobe region, crucial for the surface-based registration framework. Ground truth comparison shows accuracy with low landmark registration errors and high robustness with 89% success rate, comparable to [5]. Respiratory motion and non-rigid registration are factors which may explain the observed residual errors, and are issues which will be addressed in future work.



(a)



(b)

Fig. 2. (a) Axial and coronal slices of the segmentation result for 2 testing cases using the shape-constrained deformable model. (b) The corresponding 3D liver shapes of the 2 test cases with color coded error maps to the actual shape. The mean surface error is 0.91mm in the right liver lobe and 3.88mm in the left liver lobe.

Table 1. Error metrics from the automatically determined segmentation results for 10 datasets. The results differentiate between normal livers and fat livers, each classified based on the liver volume.

	MAD (mm)	Median (mm)	Hausdorff (mm)	DICE (%)
Normal liver (n=5)	2.1 ± 0.4	1.5 ± 0.3	12.7 ± 2.8	92.6 ± 2.2
Fat liver (n=5)	1.7 ± 0.5	1.3 ± 0.4	11.4 ± 2.7	94.5 ± 1.7
All livers (n=10)	$\mathbf{1.9 \pm 0.4}$	$\mathbf{1.4 \pm 0.3}$	$\mathbf{12.0 \pm 2.7}$	$\mathbf{93.6 \pm 2.1}$

Table 2. Average MR/US registration accuracy and precision for 4 patients, expressed with landmark registration error (LRE), and deviation of δ_t, δ_θ parameters to ground truth.

Dataset	LRE (mm)	$\delta_\theta^{mean}(\circ)$	$\delta_t^{mean}(mm)$	Success rate %
1	4.27	0.55	2.61	96
2	2.61	0.71	3.72	88
3	4.35	0.93	5.98	80
4	3.79	1.09	2.58	92
Avg. all	**3.75**	**0.90**	**3.15**	**89**

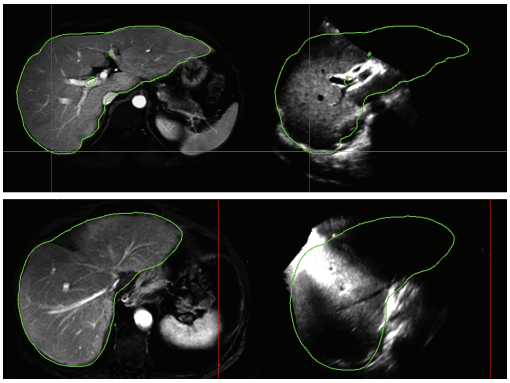


Fig. 3. Liver registration with side-by-side US and MR images (green contour shows MR liver model).

5. REFERENCES

[1] J. Kruecker, S. Xu, et al., "Clinical utility of real-time fusion guidance for biopsy and ablation," *JVIR*, pp. 515–24, 2011.

[2] A. Roche, X. Pennec, et al., "Rigid registration of 3D ultrasound with MR images: a new approach combining intensity and gradient information," *IEEE TMI*, pp. 1038–49, 2001.

[3] G. Penney, J. Blackall, M. Hamady, et al., "Registration of free-hand 3D ultrasound and magnetic resonance liver images," *Med. Imag. Anal.*, vol. 8, pp. 81–91, 2004.

[4] J. Blackall, G. Penney, A. King, and D. Hawkes, "Alignment of sparse freehand 3-D ultrasound with preoperative images of the liver using models of respiratory motion and deformation," *IEEE TMI*, vol. 24, pp. 1405–16, 2005.

[5] S. Milko, E.L. Melvaer, E. Samset, and T. Kadir, "A novel method for registration of US/MR of the liver based on the analysis of US dynamics," in *Proc. MICCAI*, 2009, pp. 771–8.

[6] G. Chen, L. Gu, L. Qian, and J. Xu, "An improved level set for liver segmentation and perfusion analysis in MRIs," *Proc. IEEE Trans Inf Technol Biomed*, vol. 3, pp. 94–103, 2009.

[7] O. Gloger, J. Kuhnb, A. Stanskic, H. Volzkea, and R. Pulsb, "A fully automatic three-step liver segmentation method on LDA-based probability maps for multiple contrast MR images," *Magn. Res. Imag.*, vol. 28, pp. 882–897, 2010.

[8] O. Ecabert, J. Peters, H. Schramm, et al., "Automatic model-based segmentation of the heart in CT images," *IEEE TMI*, vol. 27, pp. 1189–1201, 2008.

[9] J. Peters, O. Ecabert, C. Meyer, R. Kneser, and J. Weese, "Optimizing boundary detection via simulated search with applications to multi-modal heart segmentation," *Med. Imag. Anal.*, vol. 14, pp. 70–85, 2010.

[10] L. Maier-Hein, M. Schmidt, et al., "Accounting for anisotropic noise in fine registration of time-of-flight range data with high-resolution surface data," in *Proc. MICCAI*, 2010, pp. 251–8.